Environmental Boundaries as an Error Correction Mechanism for Grid Cells

Highlights

- Grid cells accumulate error relative to time and distance traveled

- Error in the grid code is corrected by encounters with environmental boundaries

- Grid error reflects systematic drift and is corrected in a direction-dependent manner

- Border cells can provide a neural substrate for error correction

Authors

Kiah Hardcastle, Surya Ganguli, Lisa M. Giocomo

Correspondence

khardcas@stanford.edu (K.H.),
giocomo@stanford.edu (L.M.G.)

In Brief

Medial entorhinal grid cells exhibit spatially periodic firing patterns and are proposed to support path integration. Hardcastle et al. found that grid cells accumulate error when animals are far from environmental boundaries and provide evidence for boundary-driven error correction.

CrossMark

CellPress

Environmental Boundaries as an Error Correction Mechanism for Grid Cells

Kiah Hardcastle,[1,*] Surya Ganguli,[1,2] and Lisa M. Giocomo[1,*]
[1]Department of Neurobiology
[2]Department of Applied Physics
Stanford University, Stanford, CA 94305, USA
*Correspondence: khardcas@stanford.edu (K.H.), giocomo@stanford.edu (L.M.G.)
http://dx.doi.org/10.1016/j.neuron.2015.03.039

SUMMARY

Medial entorhinal grid cells fire in periodic, hexagonally patterned locations and are proposed to support path-integration-based navigation. The recursive nature of path integration results in accumulating error and, without a corrective mechanism, a breakdown in the calculation of location. The observed long-term stability of grid patterns necessitates that the system either performs highly precise internal path integration or implements an external landmark-based error correction mechanism. To distinguish these possibilities, we examined grid cells in behaving rodents as they made long trajectories across an open arena. We found that error accumulates relative to time and distance traveled since the animal last encountered a boundary. This error reflects coherent drift in the grid pattern. Further, interactions with boundaries yield direction-dependent error correction, suggesting that border cells serve as a neural substrate for error correction. These observations, combined with simulations of an attractor network grid cell model, demonstrate that landmarks are crucial to grid stability.

INTRODUCTION

Since first postulated by Darwin, diverse species have been shown to use an inertia-based navigation system, commonly referred to as path integration (Bartels, 1929; Darwin, 1873; Mittelstaedt and Mittelstaedt, 1980; Wehner and Srinivasan, 1981). Path integration utilizes self-motion information, such as optic flow and proprioceptive cues, to continuously track an animal's location within its internal representation of space. For example, the cumulative integration of direction and distance traveled from a starting point can allow an animal to calculate a direct path back rather than retracing its circuitous outbound trajectory (Mittelstaedt and Mittelstaedt, 1980). The additive nature of path integration, however, inevitably results in an accumulation of error; thus, over time, the calculation of location becomes

unreliable. One strategy for accomplishing accurate navigation in the presence of path-integration-based error is landmark-based navigation, whereby animals pilot based on their location relative to familiar landmarks (Etienne, 1992). While animals can simultaneously use path integration and landmark-based navigational strategies to differing degrees, how neural circuits integrate these two modalities to support accurate navigation remains unresolved (Buzsáki and Moser, 2013; Gothard et al., 1996b; Knierim et al., 1998).

Neurons in the medial entorhinal cortex (MEC) provide many of the building blocks for creating an internal representation of self-location (Hafting et al., 2005; Sargolini et al., 2006; Solstad et al., 2008). MEC grid cells fire in periodic, hexagonally patterned locations, potentially providing a neural metric for distance traveled and a neural substrate for path integration (Fyhn et al., 2004; Hafting et al., 2005). Grid cells retain their general periodic structure across different environmental contexts and for short periods of time in darkness, suggesting that they perform online integration of self-motion cues to continuously update their estimate of location (Hafting et al., 2005). This continuous integration of self-motion cues results in a cumulative grid code, in which any error in the current estimate of position gets added to the next integrative step. The stochastic nature of neural responses, along with heterogeneous synaptic weights and a finite number of neurons, introduces sources of error that can cause an eventual breakdown in the grid code (Burak and Fiete, 2009). In simulations of attractor-based network grid cell models, grid responses break down in a few to tens of minutes, depending on the nature of the assumed noise and the size of the grid population (Burak and Fiete, 2009). If grid cells accumulate error as predicted, then a mechanism for correcting error must exist, as experimentally recorded grid patterns appear relatively stable over minutes, hours, and days (Hafting et al., 2005).

Despite computational predictions regarding grid error, accumulation of error in the grid code has never been experimentally quantified, and the potential substrates for correcting this error remain unknown. Theoretical and computational work have proposed that sensory cues regarding environmental landmarks could correct accumulated grid error, with boundaries in the environment acting as possible landmarks capable of providing an error correction signal (Burak and Fiete, 2009; Burgess, 2008; Fuhs and Touretzky, 2006; Hasselmo, 2008; McNaughton et al., 1991, 1996; Moser et al., 2008; O'Keefe and Burgess, 2005;
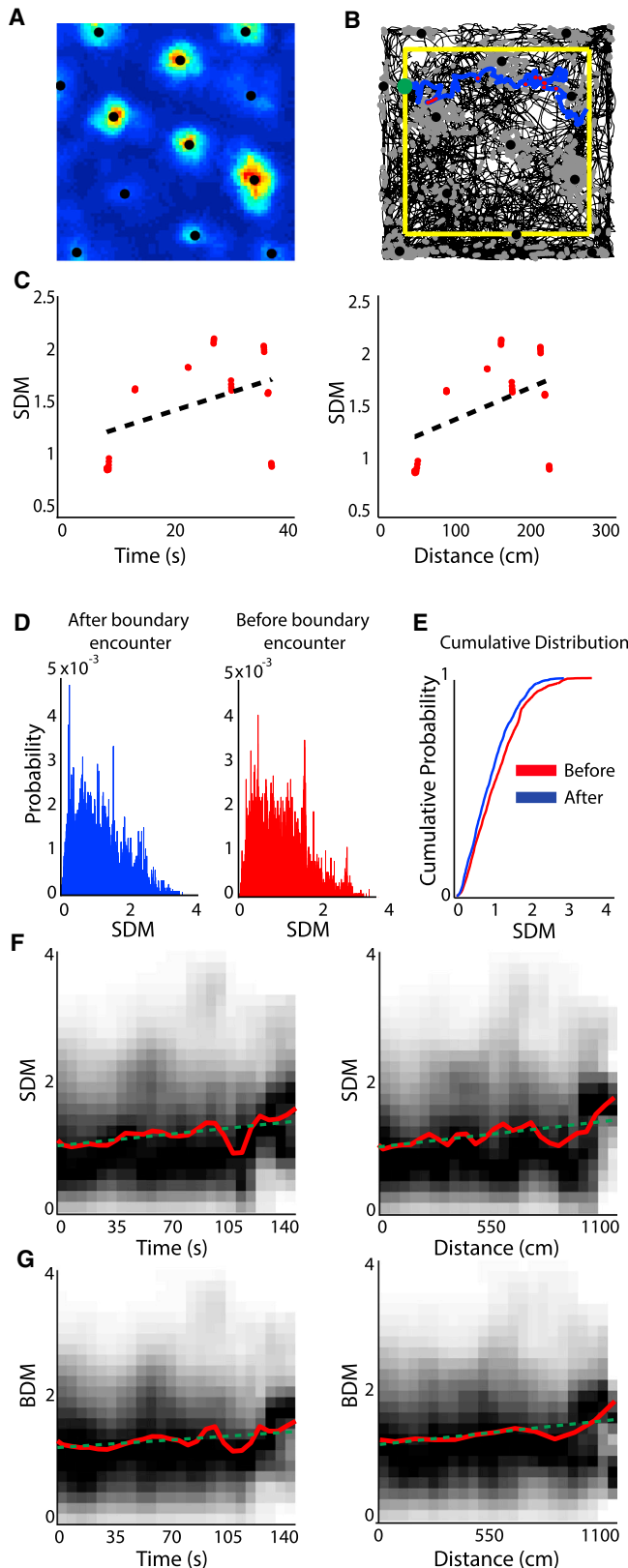
Figure 1. Error Accumulates with Time and Distance Traveled from Boundary Region

(A) Example firing rate map color coded to show minimum (blue) and maximum (red) values. Firing field COMs are in black.

(B) Example trajectory (blue) with grid cell spikes from (A) in red. The boundary region is outlined in yellow, and a green dot marks the trajectory starting point. Black lines represent trajectories over the entire session, with all spikes recorded overlaid in gray.

(C) SDM over time (left) and distance traveled (right) since the last boundary encounter for trajectory in (B).

(D) Normalized histogram of SDM for individual spikes that occurred in the 20 s after and 20 s before boundary encounters for trajectories >60 s.

(E) Cumulative distributions derived from (D).

(F) SDM for all trajectories >60 s as a function of time (left) and distance (right) traveled since the last boundary encounter. The red line is derived from a moving average of the SDM over time (left) and distance traveled (right); the green line is derived from a linear fit to the moving average. Both are overlaid on a heat map, where darker colors correspond to regions of spike density.

(G) BDM for all trajectories >60 s as a function of time (left) and distance (right) traveled since the last boundary encounter.

See also Figures S1–S4.

Redish and Touretzky, 1997; Samu et al., 2009; Savelli et al., 2008; Touretzky and Redish, 1996). Further, experimental studies have shown that the geometry of environmental boundaries can alter the structure of the grid pattern, supporting the idea that boundaries may provide input to grid cells (Barry et al., 2007; Derdikman et al., 2009; Krupic et al., 2015; Stensola et al., 2015). The neural mechanism for relaying boundary-relevant information may arise from MEC border cells, which are most active near environmental boundaries and, thus, could play a crucial role in landmark-based navigation (Barry et al., 2006; Lever et al., 2009; Savelli et al., 2008; Solstad et al., 2008). However, the role of border cells and environmental boundaries in error correction remains unknown. Here, we combine in vivo electrophysiology with computational modeling to test the idea that grid cells accumulate error and that environmental boundary information can correct this error.

RESULTS

Data Set and Definition of Boundaries

To investigate grid error accumulation and correction, we examined neural activity in the mouse MEC from two data sets (Eggink et al., 2014; Giocomo et al., 2011). We characterized the spatial coding of neurons recorded in 12 wild-type male mice with microdrives implanted in MEC as they explored a 1 m × 1 m open arena (n = 913 well-separated neurons). We classified grid cells as neurons with a grid score higher than the 99th percentile threshold (P99) determined from a shuffled distribution of grid scores (grid score threshold = 0.41) (Langston et al., 2010). To minimize the influence of directionally selective firing on our error calculation methods, we then removed cells with a head direction score >0.20 (final grid cell n = 91 from 11 mice) (Giocomo et al., 2014).

To examine the interaction between environmental features and grid coding accuracy, we compared grid spiking properties before and after mice encountered an environmental boundary. The "boundary region" was defined as the spatial area located a fixed distance from the arena edge (Figure 1B). The width of this
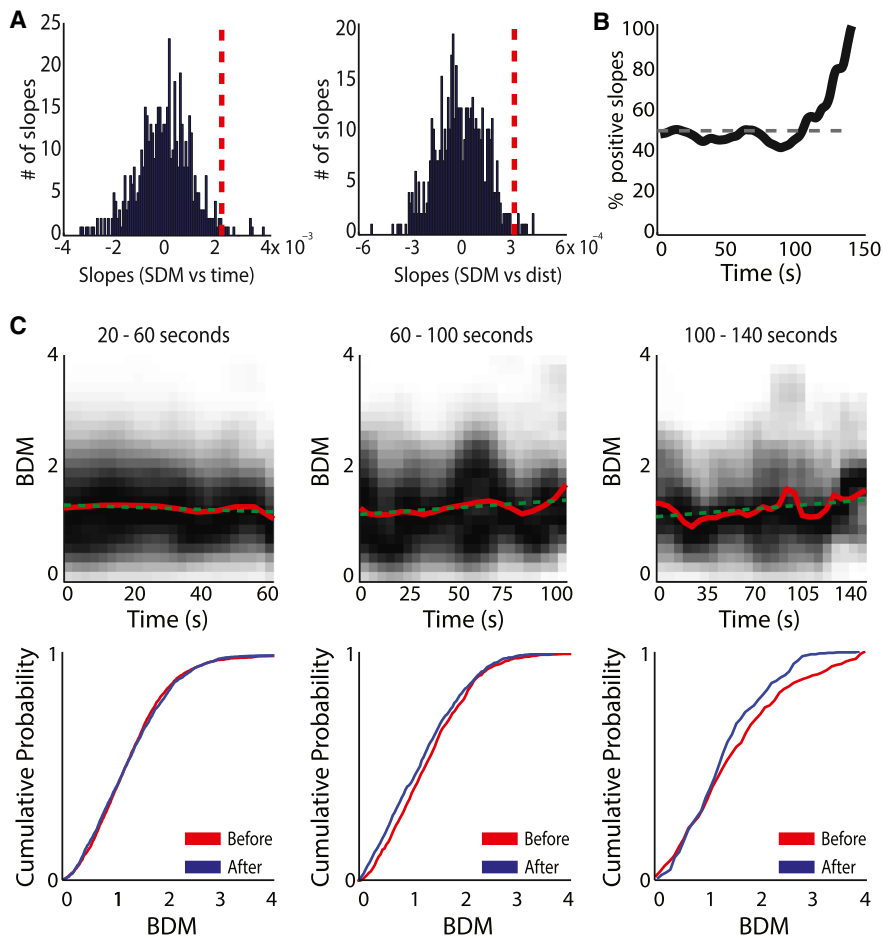
(A) The distribution of slopes for SDM versus time (left) or distance traveled (right), as generated from 500 iterations of the null data set.

(B) The number of individual trajectories with positive slopes increases with trajectory length. Each point along the y axis represents the percentage of positive slopes for trajectories with lengths greater than or equal to the corresponding time value.

(C) Top: BDM for trajectories of different lengths as a function of time traveled since the last boundary encounter. Grayscale and color coded as in Figure 1F. Bottom: cumulative distributions derived from BDM values that occurred during the first and last thirds of each trajectory following boundary encounters for trajectories shown in the top row. Color coded as in Figure 1E. 20–60 s: bursts after, n = 3,233; mean after = 1.31; bursts before, n = 3,262; mean before = 1.30; 60–100 s: bursts after, n = 1,093; mean after = 1.25; bursts before, n = 1,120; mean before = 1.37; 100–140 s: bursts after, n = 509; mean after = 1.24; bursts before, n = 510; mean before = 1.40.

icantly higher in the 20 s preceding a boundary encounter compared to the 20 s following a boundary encounter for trajectories longer than 60 s (trajectory, n = 134; grid cell, n = 64; mouse, n = 10; spikes after: n = 11,827, M = 1.12; spikes before: n = 11,725, M = 1.29; Kolmogorov-Smirnov [KS] test: K = 0.10, p < 0.001; Wilcoxon rank-sum [WRS] test: z = 16.01, p < 0.001) (Figures 1D and 1E). This result also holds when considering spike bursts (bursts after: n = 1,419, mean [M] = 1.28; bursts before: n = 1,400, M = 1.37; KS test: K = 0.06, p < 0.05; WRS test: z = 3.11, p < 0.01). These data pointed to an accumulation of grid error over long trajectories across the open portion of the arena.

Next, to examine grid error accumulation more closely, we quantified error as a function of time and distance traveled since the last boundary encounter using the SDM (Figure 1F) and BDM (Figure 1G). We found that error significantly increased relative to both time and distance traveled for the SDM and BDM (SDM, n = 50,224; BDM, n = 6,115; BDM and SDM: bootstrapping and shuffling, p < 0.01; and downsampling, p < 0.05; Figures S3B and S3C). These effects were very robust. To estimate the probability that the observed increase in error over time and distance traveled occurred by chance, we constructed a shuffled data set that preserved the rate maps and trajectories in the experimental data set but did not exhibit drift (see Experimental Procedures; Figure S3D). Using this approach, we found that the experimentally observed slope for error accumulation relative to time and distance traveled was higher than the 98th percentile of the shuffled data set (p = 0.016; Figure 2A). This indicates that the probability of observing error accumulation at the magnitude detected in the data by chance is very low.
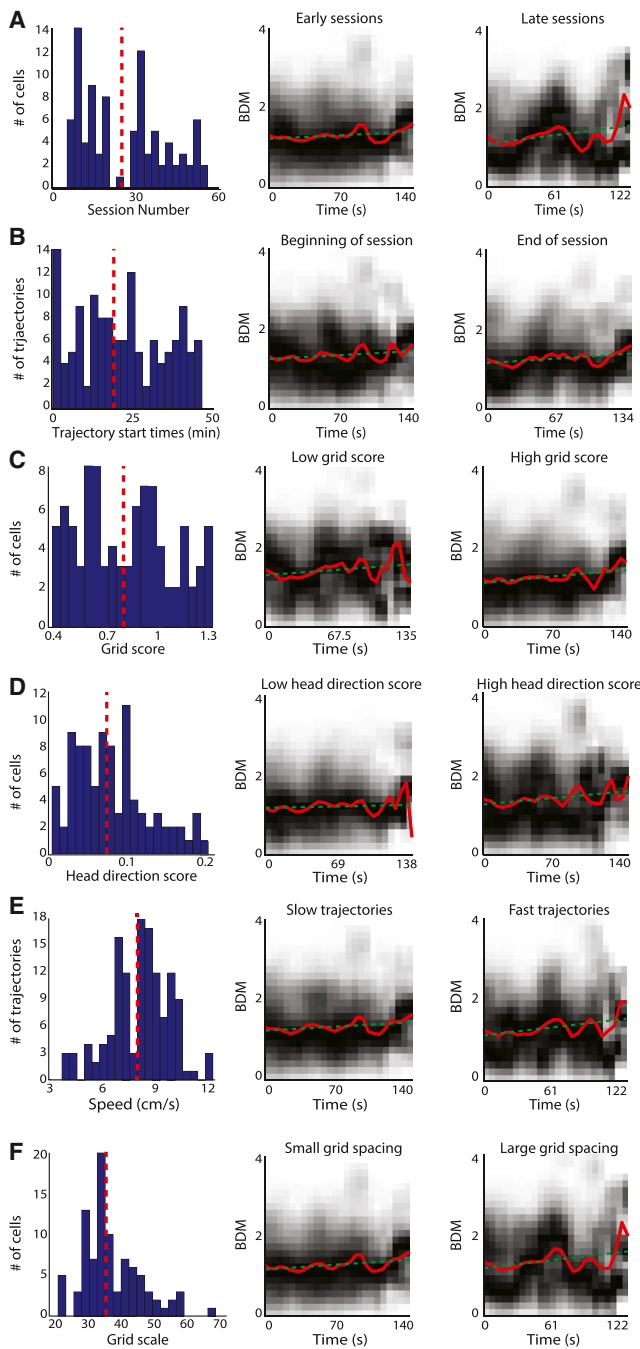
region (11 cm) was quantified based on the neural activity of MEC border cells recorded in the same 12 mice (border score > 0.6; n = 26; mice, n = 12; Figure S1). For all subsequent analyses, we considered a total of 10,557 boundary-region exit-to-entry trajectories, where the mouse exited the boundary region, traversed into the interior of the arena, and then re-entered the boundary (Figure 1; Figure S2). Spikes along these trajectories were analyzed in relation to individual grid firing fields calculated from the grid cell's activity over the entire recording session. For the purpose of this article, error correction refers to externally driven reset.

Accumulation of Grid Coding Error

First, we investigated whether grid cells accumulate significant error in the absence of environmental boundaries. To quantify error, we measured the distance of individual spikes and bursts of spikes (i.e., a spike train where each spike occurred within 20 ms of the preceding spike; Figure S3A) to the nearest grid firing field center of mass (COM). We calculated a spike distance metric (SDM) for individual spikes and a burst distance metric (BDM) for spike bursts by dividing this distance by the average radius of all firing fields for the corresponding grid cell, allowing us to compare error across different grid scales (Figures 1A–1C; Figure S5A). Using the SDM, we found that error was signif-

Figure 3. Error Accumulates Regardless of Trajectory and Grid Features

(A) Left: histogram of the number of exposures to the environment (session) for each grid cell recording. Median value (28 sessions) is indicated in red. Middle and right: BDM for trajectories in early sessions and late sessions. Early slope = 0.0010; late slope = 0.0013; comparison of slopes, F(1, 6111) = 0.17, p = 0.68. All slopes reported are BDM/s.

(B) Left: histogram of all start times. Median value (20.1 min) is indicated in red. Middle and right: BDM for trajectories in the beginning and the end of the session. Beginning slope = 0.0010; end slope = 0.0013; comparison of slopes, F(1, 6111) = 0.65, p = 0.42.

(C) Left: histogram of all grid scores. Median value (0.83) is indicated in red. Middle and right: BDM for grid cells with a grid score above and below the

Further, error accumulation was not restricted to one animal but was present in the majority of animals (five of six mice with >1 grid cell; Figure S4).

Next, we investigated the time course of error accumulation by considering temporally short, medium, and long trajectories. In this and the following analyses, we used only the BDM, as individual spikes in the SDM may be statistically dependent. When considering all individual trajectories, we observed both positive and negative slopes for linear fits to error accumulation (BDM versus time). However, as individual trajectories increased in length (>100 s), the percentage of trajectories showing a positive slope rapidly increased (Figure 2B). This increase in error accumulation for longer trajectories was reflected in the population data. We found that error significantly increased relative to time since the last boundary encounter for trajectory lengths ranging from 60 to 100 s and from 100 to 140 s, but not for trajectory lengths ranging from 20 to 60 s, as determined by bootstrapping, downsampling, and shuffling (20–60 s, all p values > 0.05; 60–100 s and 100–140 s, all p values < 0.05) and by comparing the BDM on the first and last thirds of the trajectory (20–60 s: K = 0.03, p = 0.12; 60–100 s: K = 0.08, p < 0.001; 100–140 s: K = 0.11, p < 0.01; Figure 2C). Combined, these data point to error significantly accumulating over longer times (>60 s) and raise the possibility that error does not accumulate linearly.

Error Accumulates Relative to Boundary Encounter

To investigate the nature of grid error accumulation, we considered error (BDM) for long trajectories (> 60 s) in relation to features of the trajectory and grid pattern. First, we observed an increase in grid error regardless of the number of times the animal had experienced the open arena (bootstrapping and shuffling, p < 0.01; and downsampling, p < 0.05; Figure 3A). We also observed significant error accumulation for trajectories occurring during the second half of recording sessions (bootstrapping, downsampling, and shuffling, p < 0.05; Figure 3B) and a trend toward significant error accumulation for trajectories during the first half of recording sessions (bootstrapping and shuffling, p < 0.05; downsampling, p = 0.09; Figures 3 and S5H). Additionally, error accumulated over time when considering spikes near the boundaries (<22 cm from boundary) and spikes near the center of the environment (>22 from boundary; bootstrapping, downsampling, and shuffling, p < 0.05; Figure S5D). Taken together, these data indicate that grid error

median value. High-score slope = 0.0012; low-score slope = 0.0018; comparison of slopes, F(1, 6111) = 0.92, p = 0.337.

(D) Left: histogram of all head direction scores (mean vector length; MVL). Median value (0.069) is indicated in red. Middle and right: BDM for grid cells with an MVL above and below the median value. High-MVL slope = 0.0013; low-MVL slope = 0.0010; comparison of slopes, F(1, 6111) = 0.24, p = 0.62.

(E) Left: speed for each trajectory was computed by dividing the distance traveled by the total time of the trajectory. Median value (8 cm/s) is indicated in red. Middle and right: BDM for trajectories in early sessions and late sessions. High-velocity slope = 0.0017; low-velocity slope = 0.0009; comparison of slopes, F(1, 6111) = 1.83, p = 0.18.

(F) Left: histogram of all grid scales. Median value (35 cm) is indicated in red. Middle and right: BDM for grid cells with grid spacing above and below the median value. Small-scale slope = 0.0013; large-scale slope = 0.0015.

See also Figures S5 and S6.

does not accumulate relative to time spent in the environment or absolute distance from the boundary but rather as a function of time and distance traveled since the last boundary encounter.

As the BDM assumes circular firing fields, we verified that BDM error is not due to elliptical firing fields. We found significant error accumulation in spikes associated with the most circular firing fields (aspect ratio > 0.9; bootstrapping, downsampling, and shuffling, p < 0.01; Figure S5F). Additionally, error accumulation was not restricted to cells with lower grid symmetry, as error accumulated in cells with high and low grid scores (bootstrapping and shuffling, p < 0.01; downsampling, p < 0.05; Figure 3C). Further, although we did not consider any cells with a strong directional preference, we did not observe a difference in error accumulation for the remaining cells with a comparatively high or low head direction score (bootstrapping and shuffling, p < 0.01; downsampling, p < 0.05; Figure 3D). Finally, as computational work suggests that strong velocity inputs may disrupt the grid pattern, we investigated error accumulation relative to trajectory speed (Burak and Fiete, 2009). We found significant error accumulation in both the slow and fast trajectories (bootstrapping, downsampling, and shuffling, p < 0.05; Figure 3E).

Generalization of Grid Coding Error across Scales and Species

Next, we asked if grid error accumulation is a general feature of the rodent grid network. Grid cells form functionally independent modules, with all grid cells in a module sharing the same spatial scale (Barry et al., 2007; Stensola et al., 2012). To investigate error accumulation across grid modules, we analyzed the BDM over time for different grid scales. We found that error accumulation occurred in both small- and large-scaled grid cells, suggesting that multiple grid modules accumulate error (downsampling and shuffling, p < 0.01; bootstrapping, p < 0.05; Figure 3F). Further, we did not detect a difference in the rate of error accumulation (small-scale slope = 0.0013 BDM/s, large-scale slope = 0.0015 BDM/s); comparison of slopes, F(1, 6111) = 0.13, p = 0.72. As the mean non-normalized burst distance from the nearest COM is significantly higher for large-scaled grid cells (mean BDM ± SEM: large scale, 14.3 ± 0.17 cm; small scale, 9.3 ± 0.08 cm), t(6113) = −29.5, p < 0.001, this finding suggests that the absolute spike distance from the nearest COM increases faster for large grid scales compared to small grid scales. A difference in error accumulation for different grid scales is consistent with previous work demonstrating functional independence of grid modules (Stensola et al., 2012). In attractor-network grid cell models, several factors can influence the rate of error accumulation (Burak and Fiete, 2009). First, error increases with the stochasticity of neural spiking. However, we found similar degrees of noise across small and large grid scales (Figures S6A and S6B). Second, smaller neural populations accumulate error faster, which would predict that a smaller number of grid cells compose grid modules with larger scales. Finally, if grid scale is set by the time constant of neural integration, which is consistent with previous work demonstrating dorsal-ventral gradients in the input resistance and membrane time constant of MEC neurons (Garden et al., 2008; Giocomo and Hasselmo, 2009),

error accumulation occurs faster in larger grid scales (Figures S6C and S6D).

Finally, we asked whether error accumulates across rodent species by analyzing two rat data sets (available online at http://www.ntnu.edu/kavli/research/grid-cell-data; 12 grid cells recorded in a 1.5 × 1.5 m box, trajectory n = 1,224; 23 grid cells recorded in a 1 × 1 m box, trajectory n = 1,205). To examine error, we applied the same parameters used in mice to define boundary regions, detect firing fields, and identify spike trains. We found that, similar to that for mice, rat grid error accumulated relative to time and distance traveled since the last boundary encounter (Figure 4). Collectively, these results indicate that error accumulation and correction by environmental boundaries is a general feature of rodent MEC.

Error Results from Coherent Drift of Firing Fields

The accumulation of error, combined with the absence of an increase in spike number over time and distance traveled (Figure 1D), is consistent with two distinct patterns of error accumulation: increased variance in spiking location with a fixed COM and number of spikes per firing field (Figure 5A), or drift in the grid pattern (Figure 5B). To distinguish these two possibilities, we developed a novel metric. First, we identified trajectories that passed through a grid firing field ($\overline{F}$ in Figure 5C). Then, for each field traversal, we quantified spiking in the region surrounding $\overline{F}$ by assigning values of (+1) or (−1), denoting the occurrence or absence of spikes respectively, to binary variables corresponding to field entry (α) and exit (β) (Figure 5C). For example, spiking upon firing field entry would result in $\alpha = 1$, while a lack of spiking upon firing field exit would result in $\beta = -1$. Then, we examined the product of α and β relative to the angle between field entry and exit (θ). Intuitively, for the variance model, α and β will be uncorrelated at all θ and all times, so the product $\alpha\beta$ will be constant across θ. In contrast, for the drift model, α and β will be more correlated (i.e., the same sign) at small, compared to large, θ (Figure S7). In other words, if the field has drifted, then for large θ, we expect spikes upon entry or exit—but not both—while for small θ, we expect the same behavior (either spikes or no spikes) on both entry and exit. As a result, the product $\alpha\beta$ will be a decreasing function of θ. If the magnitude of drift increases over time, then the probability of observing α and β of opposite signs at large angles will also increase, and the rate of decrease of $\alpha\beta$ with θ will increase over time (Figures S7D–S7G).

To generate quantitative, predictive values of this metric for each hypothesis, we estimated a simple linear rate of error accumulation by multiplying the slope of BDM over time (slope, 0.0012 BDM/s; best-fit line from BDM versus time for trajectories, >60 s) by the mean firing field radius (9 cm). This calculation yielded a rate of ∼0.01 cm/s, meaning that error is altering the mean grid cell spike distance from the nearest COM by ∼0.01 cm every second. Although this procedure restricts our analysis to a linear approximation of error accumulation, it allows us to calculate the predicted function $\alpha\beta(\theta)$ under each hypothesis for times both early and late in the trajectory (Figures 5D and 5E, top and bottom, respectively). To generate each predicted function at different time points, we calculated values of α and β for ensembles of trajectories that enter and exit a simulated

A Trajectory length — Trajectory length

B Trajectory speed — Trajectory speed
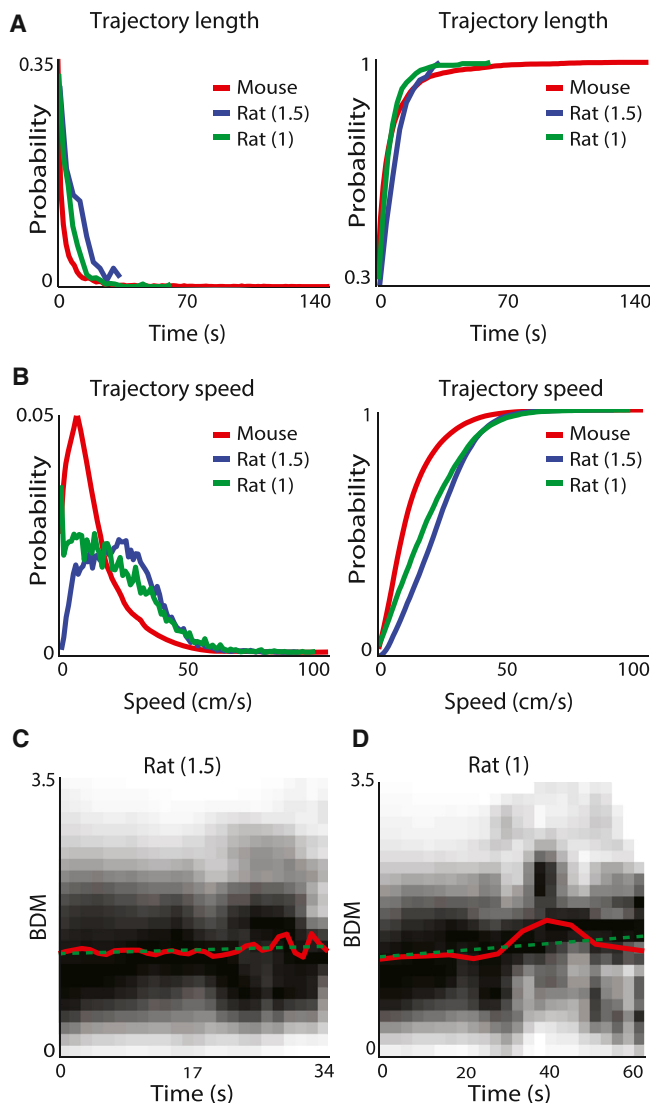
C Rat (1.5)

D Rat (1)

Figure 4. Grid Codes in Rats Accumulate Error

(A and B) The rat data set had shorter trajectories than the mouse data set, as evidenced by the normalized distribution (left) and cumulative distribution. Right: KS test for mouse and rat (1.5), K = 0.278, p < 0.001; for mouse and rat (1), K = 0.173, p < 0.001. In this data set, rats spent less time in the boundary region, as quantified by behavior during all grid cell recording sessions— mouse, 66% ± 2% of time in border; rat (1.5), 21% ± 1.5% of time in border; rat (1), 37% ± 3% of time in border; WRS tests: mouse and rat (1.5), z = −2.36, p < 0.02; mouse and rat (1), z = −4.2, p < 0.001; data not shown—and ran faster: KS test for top 10% trajectories between mouse and rat (1.5), K = 0.8918, p < 0.001; and between mouse and rat (1), K = 0.8995, p < 0.001.

(C) BDM increase over time tends toward significance for grid cells recorded from rats in the 1.5-m box (bootstrapping and shuffling, p < 0.01; down-sampling, p = 0.119). The moving average is created with a bin width of 2 s, moved 1 s along the time axis.

(D) BDM increases over time for grid cells recorded from rats in the 1-m box (all trajectories; bootstrapping, downsampling, and shuffling, p < 0.02).

firing field that has either expanded or drifted by a given amount (see Supplemental Experimental Procedures and Figure S7 for more details). Using this calculation, we found that the predicted

function $\alpha\beta(\theta)$ is constant across θ for all times under the increased variance model. For the drift model, $\alpha\beta(\theta)$ is a decreasing function, with a more significant decrease at later time points.

In the experimental data, we found that the value of $\alpha\beta$ decreases slightly over θ for early field traversals (0–30 s; field crossing, n = 6,244; shuffling, p < 0.01; Figure 5F, top), and decreases strongly over θ for later field traversals (90–120 s; field crossing, n = 62; shuffling, p < 0.05; Figure 5F, bottom). These results suggest that error accumulation results from firing fields drifting systematically over time.

Next, we asked whether the direction of drift is consistent across sequential firing field traversals. To investigate this, we identified field traversals that exhibited drift ($\alpha\beta = -1$, $\theta > \pi/4$; field traversal, n = 2,277) and preceded another field traversal (Figure 5G; Figure S7H). We identified the direction of drift in the first traversal as the angle of firing field entry or exit during which spikes occurred (a in Figure 5G). Note that this angle will not necessarily identify the precise direction that the field has drifted but serves as an estimate for the general direction of drift. We then followed these trajectories as they crossed a subsequent firing field and recorded the angle(s) at which spikes occurred during entry or exit of this field (b in Figure 5G). We found that, in many cases, the difference between these angles was small (sequential field traversal, n = 547; median less than $\pi/2$, by signed WRS test, z = −2.2091, p < 0.05) and strongest when considering sequential traversals that occurred within 10 s of each other (sequential field traversal, n = 422; median less than $\pi/2$, by signed WRS test, z = −3.0272, p < 0.01; Figure 5H). Combined, these data indicate that the observed increase in grid coding errors predominantly arises from fields systematically drifting over time. This is consistent with predictions of an attractor network model, which posits that, in the absence of corrective inputs, grid coding error results from cohesive drift in the grid cell neural sheet activity pattern (Burak and Fiete, 2009).

Boundary-Driven Error Correction

An encounter with a long, straight border is informative about positional errors perpendicular to the border but not parallel to it. For example, if the mouse encounters the north boundary, the grid network will have corrective boundary information along the north-south (NS) axis of the arena but not along the east-west (EW) axis. Thus, if boundaries in the environment correct grid error, we might expect that an encounter with a single boundary will decrease error in the perpendicular direction. This is exactly what we observed. To estimate direction-dependent error correction, we first calculated the components of Euclidean distance of each spike to the nearest COM. Next, we divided these distances by the average firing field radius, computed the mean normalized distance for each trajectory, and binned these measures according to the direction of the environmental boundary (NS or EW) the mouse had last encountered (Figures 6A and 6B). Spike accuracy (smaller SDM) increased in the NS direction after an NS, compared to an EW, boundary encounter (NS trajectory, n = 3,458; EW trajectory, n = 3,550; WRS test, z = 5.15, p < 0.001; Figure 6C). Complementary to this finding, spike accuracy increased in
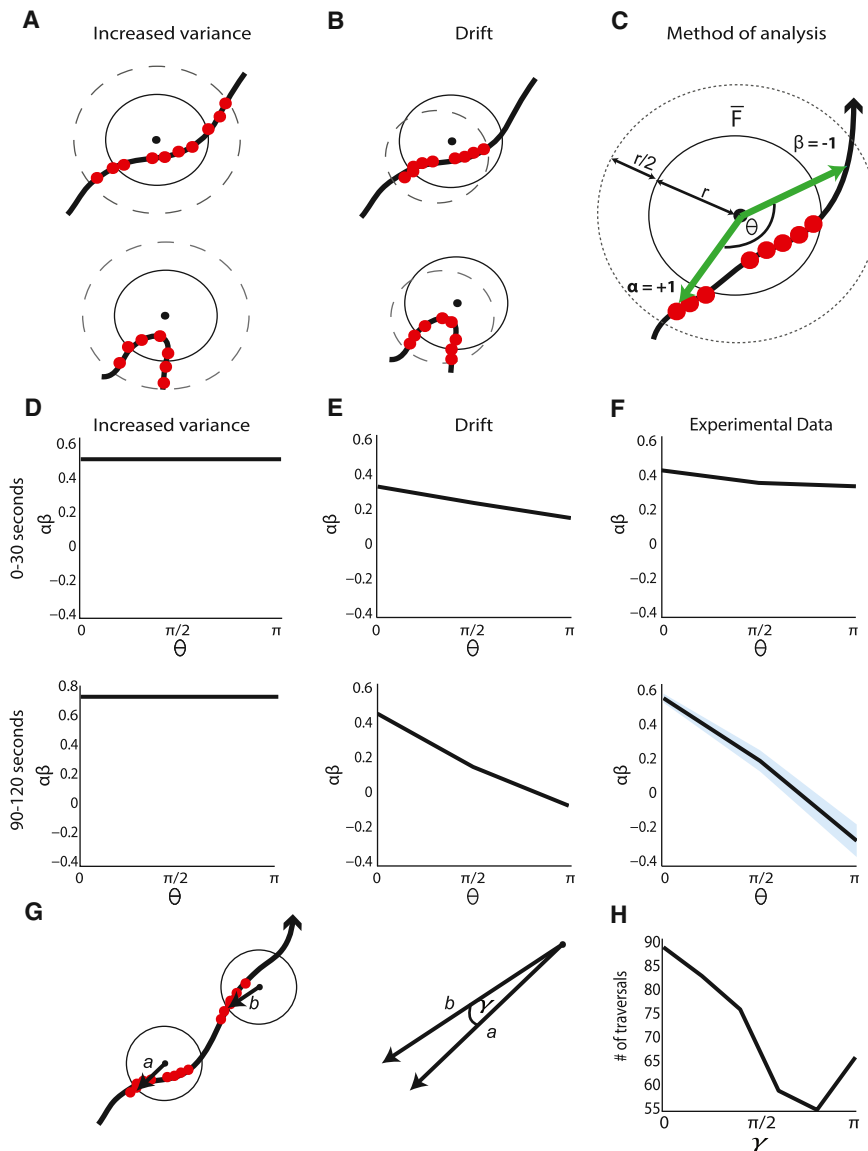
Figure 5. Error Results from Drift in the Grid Pattern

(A and B) Illustration of increased variance (A) or drift (B) over large (top) and small (bottom) entry and exit angles. Solid lines indicate the original field, and dashed lines indicate the expanded or drifted field.

(C) Schematic for analyzing out-of-field spikes, with the angle between entry and exit given by θ and field given by $\overline{F}$. The surrounding region is defined by an annulus centered on the COM, with an inner radius equal to r (solid line) and an outer radius equal to $3r/2$ (dotted line). The mean angles of entry and exit are denoted by green arrows.

(D–F) Expected dependence of $\alpha\beta$ on θ after 30 s (top) and 120 s (bottom) after exit from the boundary region for the increased variance model (D), the drift model (E), and the experimental results (F). The blue shading corresponds to the SEM (SD/square root[number of elements]).

(G) Schematic of sequential field crossings (left). The vectors a and b denote the direction of the first and second firing field entries respectively, and γ gives the angle between these vectors.

(H) A large number of sequential firing field traversals exhibited low γ, suggesting that, over short periods of time, firing fields tend to drift in the same direction.
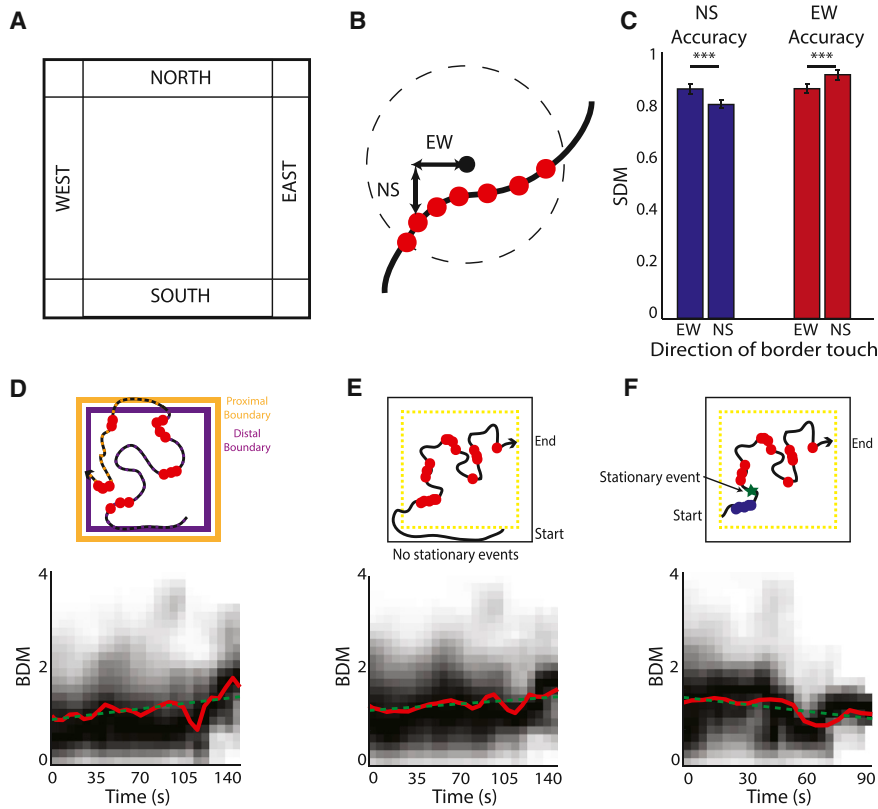
See also Figure S7.

n = 867; BDM mean after = 1.33; BDM mean before = 1.45; WRS test, z = 3.25, p < 0.001; distal boundary trajectory: n = 36, bursts after, n = 456; bursts before, n = 394; BDM mean after = 1.23; BDM mean before = 1.40; WRS test, z = 3.03, p < 0.001). Further, trajectories after either a proximal or a distal boundary encounter accumulated significant error as a function of time and distance traveled (bootstrapping, shuffling, and downsampling, p < 0.05; Figure 6D). Combined, this suggests that somatosensory contact with the arena boundary is not needed for error correction.

Finally, we noted that mice often remained stationary near the environmental boundary. Could error correction reflect times when the mouse paused to collect information about the sensory environment? To examine this question, we looked at the impact of stationary events (no movement > 5 cm/s for > 1 s) on error accumulation. We found that error accumulates over time for trajectories where a stationary event did not occur in the boundary region (trajectories > 60 s; bootstrapping and shuffling, p < 0.01; and downsampling, p < 0.05; Figure 6E). Further, error does not increase over time relative to stationary events in the open field (trajectories > 60 s; significant decrease in BDM error accumulation with bootstrapping, shuffling, and downsampling, p < 0.05; Figures 6F and S7I). Taken together, these results are consistent with the hypothesis that MEC border cells, which code for environmental

the EW direction after an EW, compared to a NS, boundary encounter (WRS test, z = 3.94, p < 0.001; Figure 6C). This result provides compelling evidence for the direct role of salient environmental landmarks—in this case, the boundaries of the open arena—in correcting grid coding error in a manner that is specific to the positional information provided by the landmark.

Next, we investigated whether somatosensory contact with boundaries is necessary for error correction. We considered long trajectories (>60 s) where the mouse either came in close proximity to the arena wall (<4 cm from wall; proximal boundary) or only entered a region distal from the arena wall (<11 cm and >7 cm from the wall; distal boundary) (Figure 6D, top). We found that the BDM was significantly higher in the 20 s prior to a boundary touch compared to the 20 s after a boundary touch for both proximal and distal boundary encounters (proximal trajectory: n = 82; bursts after, n = 856; bursts before,

Figure 6. Interactions with Boundaries Result in Direction-Dependent Error Correction

(A) Illustration of boundary wall labels. Regions of overlap were not analyzed.

(B) Illustration of quantification of EW and NS error.

(C) NS accuracy increases after an NS boundary touch, compared to an EW boundary touch, while EW accuracy increases after an EW boundary touch, compared to an NS boundary touch.

(D) Top: illustration of distal (purple) and proximal (orange) boundary regions and trajectories. Bottom: BDM increases over time for trajectories following distal boundary touches.

(E) Top: illustration of trajectories without stationary events in the boundary region. Bottom: BDM increases over time for these trajectories.

(F) Top: illustration of error calculation relative to stationary events in the open field (red spikes following stationary event). Bottom: BDM does not increase over time relative to stationary events.

See also Figure S1.

boundaries, could provide a neural substrate for boundary-driven error correction (Lever et al., 2009; Savelli et al., 2008; Solstad et al., 2008).

Implementation of Border Cell Hypothesis in an Attractor Network Model

To computationally test the idea that border cells could provide a critical input for boundary-driven error correction, we adapted a spiking attractor-network model of grid cells (Burak and Fiete, 2009). In this model, grid cells are modeled as a network of neurons with asymmetrically centered inhibitory center-surround synaptic weight profiles. Together, these neurons form a two-dimensional neural sheet upon which a grid pattern of activity appears in the presence of broad-field excitation (Figure 7A; see Supplemental Experimental Procedures for additional details). Single grid cell responses are then generated when the velocity of the animal is coupled to the movement of the neural sheet activity pattern (Burak and Fiete, 2009; Fuhs and Touretzky, 2006; Sargolini et al., 2006).

In our extension of the attractor-network model, grid cells receive excitatory input from border cells that are active near a particular border (north, south, east, or west). The activity of border cell d, B_d, that is active in region R_d is given as:

$$B_d = \begin{cases} c, & \vec{x} \in R_d \\ 0, & \vec{x} \notin R_d \end{cases}.$$

For our simulations, we take R_d to be a region near the north, south, east, or west border and $c = 1$. Input strength from

border cell d to grid cell i is proportional to the sum of that grid cell's activity over all possible positions of the animal within region R_d (Figures 7B and 7C). That is, if $r_i(\vec{x})$ denotes the firing rate of grid cell i when the animal is located at position $\vec{x}$, the synaptic weight W_{id} from border cell d to grid cell i is proportional to the integral of the grid firing rate over region R_d:

$$W_{id} = \frac{1}{N} \int_{R_d} r_i(\vec{x}) d\vec{x}.$$

N is a free parameter that scales the input. For example, the synaptic weight profile for an east border cell reflects the mean activity pattern of the neural sheet if the animal walked north along the east boundary (Figures 7B and 7C). In our simulations, we assume the presence of mature connections between border and grid cells; however, in behaving animals, these connections could develop during exploration of the open arena via a Hebbian synaptic plasticity mechanism (Widloski and Fiete, 2014).

As reported in the original model, error accumulates with time and arises from the fact that there are a finite number of stochastic neurons in the network (Burak and Fiete, 2009). In the adapted model, border cell input provides the necessary corrective mechanism to maintain accurate firing (Figures 7D–7H and S8). To give an intuition for the corrective mechanism, we turn to the one-dimensional case, i.e., a network model consisting of a neural line. At any given location, there will be a correct activity pattern across the neural line (Figure 7D). However, if the animal traverses an arena while relying on path-integration mechanisms, the animal may return to the same location with an incorrect, drifted activity pattern (Figure 7E). Restoration of the correct activity pattern may arise through activation of the subset of neurons that are supposed to be active at this location
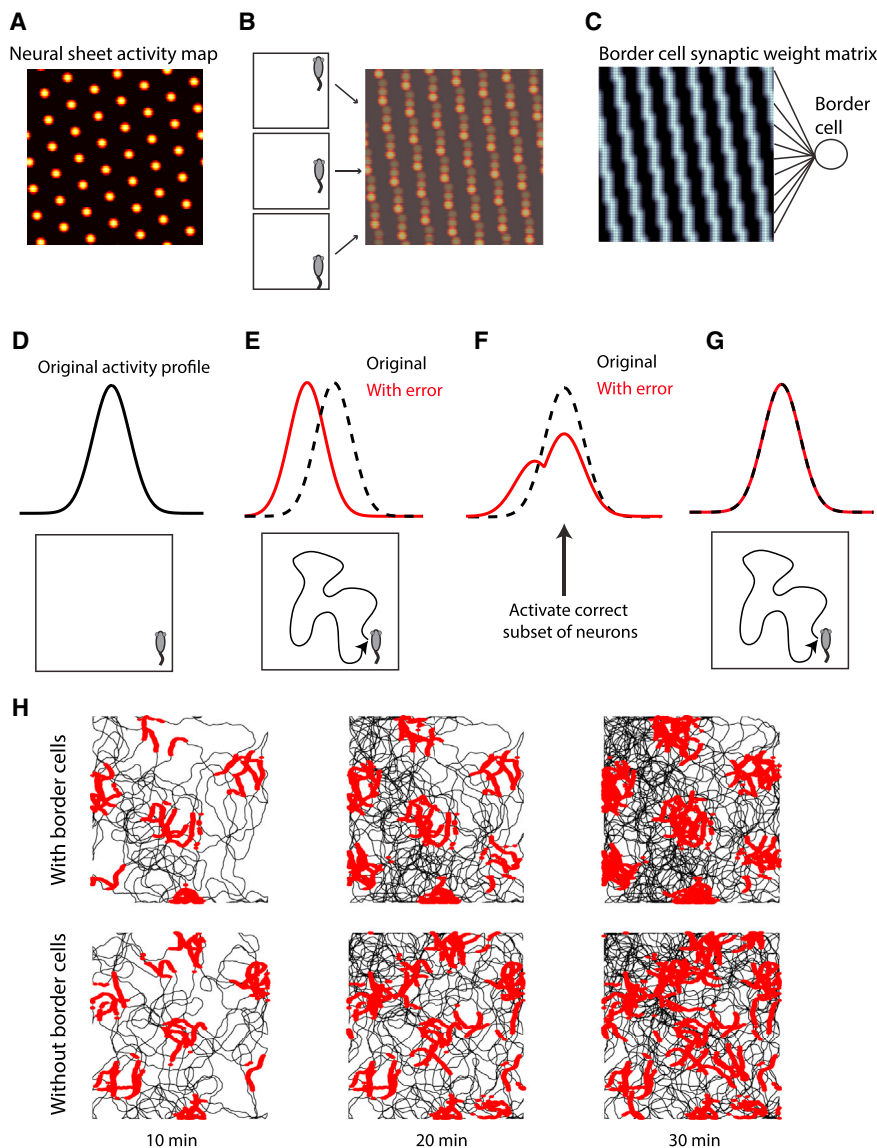
Figure 7. Attractor-Network Model with Border Cell Inputs

(A) Activity of the grid cell neural sheet (128^2 neurons, left) color coded for minimum (black) and maximum (light yellow) values for a stationary animal.

(B) Left: a mouse walks from south to north along the east border of the open arena. Right: the sum of the neural sheet activity for each location of the mouse shown on the left. This summed activity is used to generate the synaptic weight matrix for the border cell that codes for the east boundary in (C).

(C) Synaptic weight matrix for east border cell to grid cell connections color coded for minimum (black) and maximum (white) synaptic weights.

(D) Example activity pattern (black) across a one-dimensional neural line (top) at a particular location (bottom).

(E) Original example activity pattern (black, top) and incorrect drifted activity pattern (red, top) after navigation in open field (bottom).

(F) Activation of the correct subset of neurons can restore the correct activity pattern.

(G) Restoration of original activity pattern.

(H) Single-neuron output of model with (top) and without (bottom) corrective border cells over time, with trajectories in black and spikes in red.

See also Figure S8.

we analyzed the 10% longest trajectories (cell, n = 50; total trajectory, n = 3,627; trajectories >38.38 s, n = 377). We found that SDM and BDM increased with time and distance traveled since the last boundary encounter (bootstrapping, downsampling, and shuffling, p < 0.001; Figures 8D, 8E, and 8G). We also observed a direction-dependent increase in spike accuracy (NS trajectory, n = 1,760; EW trajectory, n = 1,623; NS error, WRS test, z = 10.16, p < 0.001; EW error, WRS test, z = 5.39, p < 0.001; Figure 8F). We confirmed the effect of drift over short and long time scales (for field traversal: 0–30 s, n = 2,786, p < 0.001; 60–90 s, n = 29, p < 0.05; few trajectories exceeded 90 s; Figure 8H), and observed drift in the same direction over sequential field traversals (field traversal, n = 103; difference in angle less than $\pi/2$ by signed WRS test, z = −4.49, p < 0.001; Figure 8I). As we have ground truth in the model regarding its properties of error accumulation, replication of our experimental results validates our previous analyses as a way to detect coherent drift and direction-dependent error correction. Taken together, the similarities between our simulations and the experimental data serve as a proof of principle that border cells can provide a neural mechanism for landmark-based error correction.

DISCUSSION

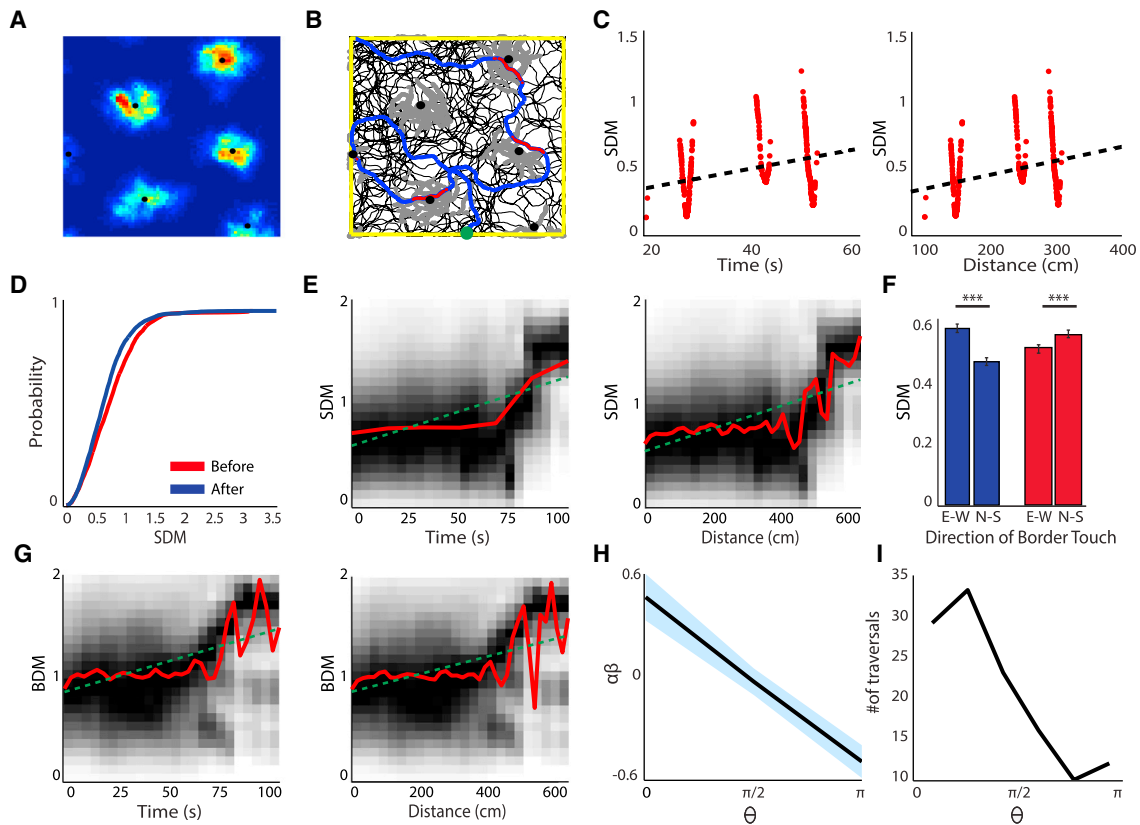Numerous theoretical and computational works propose that the grid code accumulates error, but previous experimental work

(Figure 7F). In the two-dimensional case for the east border, this subset corresponds to the neurons that are active when the animal is, at any point, along the east border. Activation of these neurons will then suppress neurons that were incorrectly active, thereby correcting accumulated error (Figure 7G). In essence, without border cell input, the grid cell network's attractor landscape has a flat, two-dimensional manifold of stable activity patterns in one-to-one correspondence with location in the open field. In the presence of border cell input, the attractor landscape tilts to move the activity pattern to the closest point on a one-dimensional family of stable activity patterns in one-to-one correspondence with locations along the associated border. This neural motion results in error correction of position coding perpendicular, but not parallel to, the border.

Our simulations using this adapted attractor-network model replicated all of our experimental results (Figure 8). Given a border region matched to the width of the simulated border cell activity,

Figure 8. Analysis of 50 Grid Cells from 10 Simulations Replicates Experimental Data

(A and B) Firing rate map for an example grid cell (A) and trajectory (B), color coded as in Figure 1.

(C) SDM over time (left) and distance traveled (right) for the trajectory in (B).

(D) The SDM is large at the end compared to beginning of long trajectories (first and last 15 s of trajectories >45 s; trajectory, n = 239; KS test, p < 0.001).

(E) SDM significantly increases over time (left) and distance traveled (right). Nonlinear increase of SDM may arise from low cell n.

(F) Direction-dependent error correction. Error bars correspond to SEM.

(G) BDM increases over time (right) and distance traveled (left).

(H and I) The value of $\alpha\beta$ decreases with θ for field traversals 60–90 s after a boundary region exit (H), and firing fields tend to drift in the same direction (I).

has neither directly tested this nor quantified error accumulation and its dependence on landmarks. By taking advantage of a large data set of grid cell recordings in behaving rodents, we were able to analyze thousands of trajectories and find paths long enough to examine grid error accumulation. Our results demonstrate that grid cells accumulate significant error in the absence of input from environmental boundaries. This error accumulates with an initial rate of approximately 0.01 cm/s, which, if left uncorrected, would lead to a complete breakdown of the grid code within tens of minutes. Our study further suggests that error results from coherent drift in the grid pattern, an observation consistent with predictions on the nature of error accumulation by attractor-based network grid cell models (Burak and Fiete, 2009; Roudi and Treves, 2008; Zhang, 1996). Finally, the direction-dependent correction of drift, combined with results from our computational simulations, raises the possibility that border cells provide a neural substrate for error correction.

Several features of border cells highlight them as a neural population well suited to support grid error correction.

First, they develop spatial coding properties before grid cells, providing one of the earliest stable codes of the external environment (Bjerknes et al., 2014; Langston et al., 2010; Wills et al., 2010). The early stability of border cells may also be one reason for the observed reset of hippocampal place cells after an animal encounters an environmental boundary (Barry et al., 2006; Gothard et al., 1996a, 2001; Zhang et al., 2014). Second, the intermingled nature of border and grid cells indicates anatomical proximity, which could facilitate synaptic plasticity between the two populations and support border-driven error correction as predicted by our computational simulations (McNaughton and Nadel, 1991; Solstad et al., 2008; Widloski and Fiete, 2014). Additionally, landmark-driven error correction through classic Hebbian learning rules has been implemented in models of other spatially selective cells, such as head direction cells (McNaughton et al., 1991; Skaggs et al., 1995; Zhang, 1996). Finally, unlike that for hippocampal place cells, the spatial location of border cell firing generalizes across a number of environmental geometries, reducing the number of new associations between error-correction inputs and grid cells needed to code accurately

across different environments (Leutgeb et al., 2005a, 2005b; Savelli et al., 2008; Solstad et al., 2008).

The nature of error accumulation in the grid code has implications for computational models and theoretical considerations of the grid cell network. Attractor-based network models specifically predict that grid coding error results from imprecise tracking of the grid pattern across the neural sheet with the movement of the animal (Burak and Fiete, 2009). However, the use of landmarks to correct error in the grid code should extrapolate to other computational models of grid cell formation (Burgess et al., 2007; Bush and Burgess, 2014; Kropff and Treves, 2008). In particular, recent theoretical work has shown that, regardless of grid cell model type, the population-level grid code is particularly robust against single-cell noise (Sreenivasan and Fiete, 2011). This suggests that the observed error accumulation in the grid code may result primarily from error common to all grid cells within the network, with input regarding external landmarks providing a method to systematically eradicate this network error.

The interaction between environmental boundaries and error correction implies that sensory input and animal behavior influence grid coding in a manner consistent with previous computational predictions (Burak and Fiete, 2009; McNaughton et al., 1991, 2006; Samsonovich and McNaughton, 1997; Skaggs et al., 1995; Zhang, 1996). First, our results suggest that the navigational trajectories of an animal can determine how well grid cells code the environment. Second, our experimental environment drastically differs from the cue-rich environment that an animal experiences in the wild. In the real world, various physical objects form boundaries that constrain an animal's movement and serve as stable landmarks. Our computational work indicates that any external sensory feature that activates border cells can correct error. This suggests that, for accurate grid representations to emerge in a more natural environment, a wider variety of sensory cues would need to activate the border cell population. Consistent with this idea, border cells have been shown to code for boundaries characterized by a drop rather than a wall, short boundary walls over which the animal can still navigate and in primates, the edges of an image presentation screen (Barry et al., 2006; Killian et al., 2012; Lever et al., 2009; Solstad et al., 2008). The possibility also remains that neurons that code for other environmental features, such as lateral entorhinal object cells, could provide an additional error correction signal in more complex environments (Deshmukh and Knierim, 2011; Tsao et al., 2013).

Taken together, these data provide evidence of error accumulation and correction within the grid network. The strong dependence of grid stability on landmark information suggests that, if grid cells serve as the neural substrate for path integration, sensory input must play a key role in generating an accurate estimate of location. One challenge that must be overcome for sensory-based error correction in the grid code is the neural location of the grid network, which lies several synapses away from primary sensory receptors. The utilization of local MEC border cell activity as a substrate for error correction points to a fundamental role of local circuit dynamics in supporting noise-robust representations in higher order non-sensory cortical regions. Further, the possibility remains that grid cells represent a higher order spatial memory code beyond the implementation of path integration (Buzsáki and Moser, 2013). However, regardless of the role of grid cells in memory or navigation, drift-based error would constitute a source of uncertainty; thus, the presence of a corrective mechanism would be crucial for the grid network to accurately code either spatial or memory-related variables.

EXPERIMENTAL PROCEDURES

Trajectories
Trajectories were identified as paths taken by the animal as it exited and re-entered the boundary region. "Time = 0" and "distance traveled = 0" correspond to the moment the animal left the defined boundary region. Time and distance traveled points are then calculated until the animal re-enters the boundary region. The majority of these trajectories are temporally short (82% are <10 s). However, the presence of a coherent grid map in the middle of the arena indicates that significant grid error accumulation in less than 10 s is unlikely. Further, the presence of a large number of short trajectories supports our assumption that the average spatial firing rate is a nearly error-free grid representation, allowing us to quantify error by comparing the spikes associated with long trajectories with the average spiking pattern. Thus, we primarily considered only trajectories >60 s, unless noted otherwise.

Firing Field Detection
We used an adaptive smoothed rate map to identify firing fields (Skaggs et al., 1996). Fields were detected as connected regions with a total area greater than ten bins ($\sim$20 cm^2), where each bin had a firing rate in the 75th percentile (determined by the cumulative distribution function [CDF]) of binned firing rates for that rate map.

The center of mass of each firing field is given as:

$$COM_x = \frac{\sum_{i=1}^{N} FR_i * x_i}{\sum_{i=1}^{N} FR_i}$$

and

$$COM_y = \frac{\sum_{i=1}^{N} FR_i * y_i}{\sum_{i=1}^{N} FR_i},$$

where N is the number of bins, FR_i is the firing rate for bin i, and x_i and y_i are the x and y positions of bin i. The firing field radius is computed as the radius of the circle with an area equal to the firing field area.

Burst Distance Metric
To identify spike bursts, we compute the mean time and mean SDM for spikes that occur within 20 ms of each other. Identified spike trains contained 2–170 spikes (mean 8 ± 7 spikes; Figure S3A).

Visualization of Data
Lines depicting moving averages are created by taking the mean of a bin 10 s long or 80 cm wide, moved along the x axis in steps of 5 s or 40 cm for time and distance plots, respectively (unless otherwise noted). Heat maps are created by binning the plane into 25^2 bins (25 bins along both the x and y axes), and counting the number of spikes in each bin. High-frequency noise in the spike count is removed with a 4 × 4 Gaussian filter (σ = 2), and the columns (fixed time or distance bins) are normalized to adjust for differences in spike number. This map is then grayscale coded; black corresponds to bins with maximum spike number, and white corresponds to bins without spikes (Figures 1, 2, 3, 4, 6, 8, and S5).

Statistical Analyses
To test the statistical significance of the observed slopes, we applied three procedures to the raw data: bootstrapping, downsampling, and shuffling.
Bootstrapping
We resampled with replacement from the original data set. The number of samples drawn on each bootstrap iteration was equal to the number of

points in the original data set. For each iteration, we fit a first-order polynomial through the method of ordinary least-squares to the new resampled data set and recorded the slope of the best-fit line as the sample statistic. This procedure was iterated 10,000 times, and the resulting p value was derived as the probability of observing a positive slope.

Downsampling

We first divided the data points along time or distance traveled into n bins. Bin widths were chosen to be the maximal number of bins so that every bin contained at least 10% of the data points. We then sampled k points from all bins, where k is the minimum number of points in a bin, and fit a line through the ordinary least-squares method to the mean value of each bin. This procedure was carried out 10,000 times, and the resulting p value was associated with the probability of observing a positive slope (as in the bootstrapping method).

Shuffling

To create a shuffled data set, each original data point was randomly assigned a new value along the x axis, chosen from the set of x axis values in the original data set. A first-order polynomial was then fit through the method of ordinary least-squares. This procedure was carried out 10,000 times, generating a distribution of slope values. The resulting p value associated with observing a slope of a given magnitude by chance is then calculated as the proportion of slopes from the distribution of shuffled data with a value greater than or equal to the observed slope.

Null Data Set

To construct null distributions of SDM versus time and distance-traveled slopes, we generated 500 non-error accumulating (null) data sets for SDM versus time and SDM versus distance traveled. Each null data set contains SDM data from 91 model grid cells, where each cell is constructed by matching the firing rate map of one grid cell with a randomly chosen position file from a different recording session. To generate a new set of spikes for each model grid cell, we used the original firing map as a Poisson rate function for spiking in the locations determined by the randomly chosen position file. We were then able to determine the normalized distance of simulated Poisson spikes from the nearest center of mass (determined by the original rate map) along each trajectory >60 s as a function of time and distance traveled from the boundary region. We then repeated this process for the original 91 grid cell firing rate maps to construct one null data set (and one slope for SDM versus time and SDM versus distance).

To test the similarity between slopes of two or more data sets, we applied a univariate analysis of covariance (ANCOVA) using the MATLAB Analysis of Covariance Tool (aoctool). For each test, we fit the model using separate lines. Significant differences in two slopes were detected with the ANCOVA test statistic, reported as: F(degrees of freedom of x axis, degrees of freedom of error) = F statistic. Differences in group medians were detected using the nonparametric WRS test. Differences in group distributions were detected using the KS test.

Drift Calculation

For each grid cell, we define the region surrounding a firing field as r to $3r/2$ from the COM, where r is the average radius of all firing fields for that cell. To generate predictions of the dependence of $\alpha\beta$ on the angle θ for each hypothesis, we modeled a firing field as a two-dimensional Gaussian function constrained by the mean firing field peak and radius and calculated $\alpha\beta = P_e P_x + (1 - P_e)(1 - P_x) - ((1 - P_e)P_x + (1 - P_x)P_e)$ for exit and entry trajectories separated by angle θ. P_e denotes the probability of spiking during entry, and P_x denotes the probability of spiking during exit.

Direction-Dependent Error Calculation

We characterized the type of boundary encounter by dividing the boundary region into eight regions: north, south, east, west, NE, SE, SW, and SE. For our analysis, we considered the first four types of boundary encounters (Figure 5A). We computed the mean normalized x (EW) and y (NS) spike distance from the COM for each trajectory.

Implementation of Attractor Network Model

Model implementations were generated in MATLAB. For our simulations, we adapted a spiking model with periodic boundary conditions as described by Burak and Fiete (2009) (see Supplemental Experimental Procedures).

REFERENCES

Barry, C., Lever, C., Hayman, R., Hartley, T., Burton, S., O'Keefe, J., Jeffery, K., and Burgess, N. (2006). The boundary vector cell model of place cell firing and spatial memory. Rev. Neurosci. *17*, 71–97.

Barry, C., Hayman, R., Burgess, N., and Jeffery, K.J. (2007). Experience-dependent rescaling of entorhinal grids. Nat. Neurosci. *10*, 682–684.

Bartels, M. (1929). Sinnesphysiologische und psychologische Untersuchungen an der Trichterspinne *Agelena labyrinthica* (Cl.). Z. Vgl. Physiol. *10*, 527–593.

Bjerknes, T.L., Moser, E.I., and Moser, M.B. (2014). Representation of geometric borders in the developing rat. Neuron *82*, 71–78.

Burak, Y., and Fiete, I.R. (2009). Accurate path integration in continuous attractor network models of grid cells. PLoS Comput. Biol. *5*, e1000291.

Burgess, N. (2008). Grid cells and theta as oscillatory interference: theory and predictions. Hippocampus *18*, 1157–1174.

Burgess, N., Barry, C., and O'Keefe, J. (2007). An oscillatory interference model of grid cell firing. Hippocampus *17*, 801–812.

Bush, D., and Burgess, N. (2014). A hybrid oscillatory interference/continuous attractor network model of grid cell firing. J. Neurosci. *34*, 5065–5079.

Buzsáki, G., and Moser, E.I. (2013). Memory, navigation and theta rhythm in the hippocampal-entorhinal system. Nat. Neurosci. *16*, 130–138.

Darwin, C. (1873). Origin of certain instincts. Nature *7*, 417–418.

Derdikman, D., Whitlock, J.R., Tsao, A., Fyhn, M., Hafting, T., Moser, M.B., and Moser, E.I. (2009). Fragmentation of grid cell maps in a multicompartment environment. Nat. Neurosci. *12*, 1325–1332.

Deshmukh, S.S., and Knierim, J.J. (2011). Representation of non-spatial and spatial information in the lateral entorhinal cortex. Front. Behav. Neurosci. *5*, 69.

Eggink, H., Mertens, P., Storm, I., and Giocomo, L.M. (2014). HCN1 independent grid cell phase precession in mice. Hippocampus *24*, 249–256.

Etienne, A.S. (1992). Navigation of a small mammal by dead reckoning and local cues. Curr. Dir. Psychol. Sci. *1*, 48–52.

Fuhs, M.C., and Touretzky, D.S. (2006). A spin glass model of path integration in rat medial entorhinal cortex. J. Neurosci. *26*, 4266–4276.

Fyhn, M., Molden, S., Witter, M.P., Moser, E.I., and Moser, M.B. (2004). Spatial representation in the entorhinal cortex. Science *305*, 1258–1264.

Garden, D.L., Dodson, P.D., O'Donnell, C., White, M.D., and Nolan, M.F. (2008). Tuning of synaptic integration in the medial entorhinal cortex to the organization of grid cell firing fields. Neuron *60*, 875–889.

Giocomo, L.M., and Hasselmo, M.E. (2009). Knock-out of HCN1 subunit flattens dorsal-ventral frequency gradient of medial entorhinal neurons in adult mice. J. Neurosci. *29*, 7625–7630.

Giocomo, L.M., Hussaini, S.A., Zheng, F., Kandel, E.R., Moser, M.B., and Moser, E.I. (2011). Grid cells use HCN1 channels for spatial scaling. Cell *147*, 1159–1170.

Giocomo, L.M., Stensola, T., Bonnevie, T., Van Cauter, T., Moser, M.B., and Moser, E.I. (2014). Topography of head direction cells in medial entorhinal cortex. Curr. Biol. *24*, 252–262.

Gothard, K.M., Skaggs, W.E., and McNaughton, B.L. (1996a). Dynamics of mismatch correction in the hippocampal ensemble code for space: interaction between path integration and environmental cues. J. Neurosci. *16*, 8027–8040.

Gothard, K.M., Skaggs, W.E., Moore, K.M., and McNaughton, B.L. (1996b). Binding of hippocampal CA1 neural activity to multiple reference frames in a landmark-based navigation task. J. Neurosci. *16*, 823–835.

Gothard, K.M., Hoffman, K.L., Battaglia, F.P., and McNaughton, B.L. (2001). Dentate gyrus and ca1 ensemble activity during spatial reference frame shifts in the presence and absence of visual input. J. Neurosci. *21*, 7284–7292.

Hafting, T., Fyhn, M., Molden, S., Moser, M.B., and Moser, E.I. (2005). Microstructure of a spatial map in the entorhinal cortex. Nature *436*, 801–806.

Hasselmo, M.E. (2008). Grid cell mechanisms and function: contributions of entorhinal persistent spiking and phase resetting. Hippocampus *18*, 1213–1229.

Killian, N.J., Jutras, M.J., and Buffalo, E.A. (2012). A map of visual space in the primate entorhinal cortex. Nature *491*, 761–764.

Knierim, J.J., Kudrimoti, H.S., and McNaughton, B.L. (1998). Interactions between idiothetic cues and external landmarks in the control of place cells and head direction cells. J. Neurophysiol. *80*, 425–446.

Kropff, E., and Treves, A. (2008). The emergence of grid cells: Intelligent design or just adaptation? Hippocampus *18*, 1256–1269.

Krupic, J., Bauza, M., Burton, S., Barry, C., and O'Keefe, J. (2015). Grid cell symmetry is shaped by environmental geometry. Nature *518*, 232–235.

Langston, R.F., Ainge, J.A., Couey, J.J., Canto, C.B., Bjerknes, T.L., Witter, M.P., Moser, E.I., and Moser, M.B. (2010). Development of the spatial representation system in the rat. Science *328*, 1576–1580.

Leutgeb, J.K., Leutgeb, S., Treves, A., Meyer, R., Barnes, C.A., McNaughton, B.L., Moser, M.B., and Moser, E.I. (2005a). Progressive transformation of hippocampal neuronal representations in "morphed" environments. Neuron *48*, 345–358.

Leutgeb, S., Leutgeb, J.K., Barnes, C.A., Moser, E.I., McNaughton, B.L., and Moser, M.B. (2005b). Independent codes for spatial and episodic memory in hippocampal neuronal ensembles. Science *309*, 619–623.

Lever, C., Burton, S., Jeewajee, A., O'Keefe, J., and Burgess, N. (2009). Boundary vector cells in the subiculum of the hippocampal formation. J. Neurosci. *29*, 9771–9777.

McNaughton, B.L., and Nadel, L. (1991). Hebb-Marr networks and the neurobiological representation of action in space. In Neuroscience and Connectionist Theory, M.A. Gluck and D.E. Rumelhart, eds. (Hillsdale, NJ: Erlbaum), pp. 1–64.

McNaughton, B.L., Chen, L.L., and Markus, E.J. (1991). "Dead reckoning," landmark learning, and the sense of direction: a neurophysiological and computational hypothesis. J. Cogn. Neurosci. *3*, 190–202.

McNaughton, B.L., Barnes, C.A., Gerrard, J.L., Gothard, K., Jung, M.W., Knierim, J.J., Kudrimoti, H., Qin, Y., Skaggs, W.E., Suster, M., and Weaver, K.L. (1996). Deciphering the hippocampal polyglot: the hippocampus as a path integration system. J. Exp. Biol. *199*, 173–185.

McNaughton, B.L., Battaglia, F.P., Jensen, O., Moser, E.I., and Moser, M.B. (2006). Path integration and the neural basis of the 'cognitive map'. Nat. Rev. Neurosci. *7*, 663–678.

Mittelstaedt, M., and Mittelstaedt, H. (1980). Homing by path integration in a mammal. Naturwissenschaften *67*, 566–567.

Moser, E.I., Kropff, E., and Moser, M.B. (2008). Place cells, grid cells, and the brain's spatial representation system. Annu. Rev. Neurosci. *31*, 69–89.

O'Keefe, J., and Burgess, N. (2005). Dual phase and rate coding in hippocampal place cells: theoretical significance and relationship to entorhinal grid cells. Hippocampus *15*, 853–866.

Redish, A.D., and Touretzky, D.S. (1997). Cognitive maps beyond the hippocampus. Hippocampus *7*, 15–35.

Roudi, Y., and Treves, A. (2008). Representing where along with what information in a model of a cortical patch. PLoS Comput. Biol. *4*, e1000012.

Samsonovich, A., and McNaughton, B.L. (1997). Path integration and cognitive mapping in a continuous attractor neural network model. J. Neurosci. *17*, 5900–5920.

Samu, D., Eros, P., Ujfalussy, B., and Kiss, T. (2009). Robust path integration in the entorhinal grid cell system with hippocampal feed-back. Biol. Cybern. *101*, 19–34.

Sargolini, F., Fyhn, M., Hafting, T., McNaughton, B.L., Witter, M.P., Moser, M.B., and Moser, E.I. (2006). Conjunctive representation of position, direction, and velocity in entorhinal cortex. Science *312*, 758–762.

Savelli, F., Yoganarasimha, D., and Knierim, J.J. (2008). Influence of boundary removal on the spatial representations of the medial entorhinal cortex. Hippocampus *18*, 1270–1282.

Skaggs, W.E., Knierim, J.J., Kudrimoti, H.S., and McNaughton, B.L. (1995). A model of the neural basis of the rat's sense of direction. Adv. Neural Inf. Process. Syst. *7*, 173–180.

Skaggs, W.E., McNaughton, B.L., Wilson, M.A., and Barnes, C.A. (1996). Theta phase precession in hippocampal neuronal populations and the compression of temporal sequences. Hippocampus *6*, 149–172.

Solstad, T., Boccara, C.N., Kropff, E., Moser, M.B., and Moser, E.I. (2008). Representation of geometric borders in the entorhinal cortex. Science *322*, 1865–1868.

Sreenivasan, S., and Fiete, I. (2011). Grid cells generate an analog error-correcting code for singularly precise neural computation. Nat. Neurosci. *14*, 1330–1337.

Stensola, H., Stensola, T., Solstad, T., Frøland, K., Moser, M.B., and Moser, E.I. (2012). The entorhinal grid map is discretized. Nature *492*, 72–78.

Stensola, T., Stensola, H., Moser, M.B., and Moser, E.I. (2015). Shearing-induced asymmetry in entorhinal grid cells. Nature *518*, 207–212.

Touretzky, D.S., and Redish, A.D. (1996). Theory of rodent navigation based on interacting representations of space. Hippocampus *6*, 247–270.

Tsao, A., Moser, M.-B., and Moser, E.I. (2013). Traces of experience in the lateral entorhinal cortex. Curr. Biol. *23*, 399–405.

Wehner, R., and Srinivasan, M.V. (1981). Searching behavior of desert ants, genus *Cataglyphis* (Formicidae, Hymenoptera). J. Comp. Physiol. *142*, 315–338.

Widloski, J., and Fiete, I.R. (2014). A model of grid cell development through spatial exploration and spike time-dependent plasticity. Neuron *83*, 481–495.

Wills, T.J., Cacucci, F., Burgess, N., and O'Keefe, J. (2010). Development of the hippocampal cognitive map in preweanling rats. Science *328*, 1573–1576.

Zhang, K. (1996). Representation of spatial orientation by the intrinsic dynamics of the head-direction cell ensemble: a theory. J. Neurosci. *16*, 2112–2126.

Zhang, S.J., Schönfeld, F., Wiskott, L., and Manahan-Vaughan, D. (2014). Spatial representations of place cells in darkness are supported by path integration and border information. Front. Behav. Neurosci. *8*, 222.